Batteries & Supercaps

Research Article
doi.org/10.1002/batt.202300351

Chemistry Europe
European Chemical
Societies Publishing

www.batteries-supercaps.org

Interaction Mechanisms Between Nitrogen-Containing Groups and Alkali Metals with Molecular Model System of HATCN**

Yuan Liu,[a, b] Xu Lian,[b, c] Xiaojiang Yu,[d] Yuxiang Niu,[b] Jinlin Yang,*[b] Yishui Ding,[a, b] and Wei Chen*[a, b, e]

To enable the practical implementation of alkali metal batteries (AMBs), significant endeavors have been focused on enhancing the stability of alkali metal anodes (AMAs) using a range of strategies, such as optimizing electrolyte compositions, constructing anode deposition hosts, and establishing artificial protective layers. Despite significant progress in enhancing battery performance, limited attention has been given to comprehending the interaction mechanisms between alkali metals and protective materials, which is pivotal for the informed development of novel protective materials. Thus, aiming to enhance the comprehension of interaction processes between AMAs and organic protective materials containing various nitrogen groups, we conducted a mechanism study utilizing 1,4,5,8,9,11-hexaazatriphenylenehexacarbonitrile (HATCN) as the model material, based on *in-situ* x-ray and ultraviolet photoelectron spectroscopy (XPS/UPS), and near edge x-ray absorption fine structure (NEXAFS), as well as density functional theory (DFT) calculations. Through the investigation of interaction processes between HATCN and Li/Na, we find that Li or Na interacts with the two different nitrogen-containing groups of HATCN in the same order: preferentially interacts with the inner imine groups of HATCN before interacting with the outer nitrile groups. Interestingly, our findings also reveal that the two distinct nitrogen-containing groups exhibit a smaller difference in their sodiophilicity compared to their difference in lithiophilicity. These valuable insights shed light on the intricate interactions between nitrogen-containing protective materials and AMAs, paving the way for the development of more effective protective materials in the future.

Introduction

Given the growing need for high-energy storage systems, significant efforts have been directed toward the advancement of rechargeable batteries. Notably, the current market includes prevalent alkali metal ion batteries (AIBs) like lithium-ion and sodium-ion batteries, which find extensive application in portable electronic devices, electric vehicles, and grid energy storage systems.[1] The development of AIBs involves the exploration of various anode materials to accommodate alkali ions during cycling, encompassing commercial graphite, alloy-type substances, and innovative organic materials, among others.[2] These anode materials in batteries tend to impose limitations on their energy densities. In the pursuit of achieving higher energy densities, alkali metal batteries (AMBs) have emerged as a focal point of research and development owing to their low redox potential (Li: −3.04 V vs. standard hydrogen electrode (SHE); Na: −2.71 V vs. SHE) and remarkable theoretical capacity (Li: 3860 mAh/g; Na: 1166 mAh/g).[3] However, utilizing alkali metals directly as anodes poses several challenges that hinder the practical application of AMBs. On one hand, the inherent reactivity of alkali metals results in problematic side reactions with various electrolyte compositions, leading to the formation of unstable solid-electrolyte interphases (SEIs).[4] These SEIs exhibit high interfacial resistance that worsens over time, even under static conditions.[5] Additionally, the substantial volume changes caused by hostless alkali metal deposition can cause the fragile SEIs to develop cracks during cycling,

[a] Dr. Y. Liu, Y. Ding, Prof. Dr. W. Chen
    Joint School of National University of Singapore and Tianjin University,
    International Campus of Tianjin University,
    Binhai New City, Fuzhou 350207, PR China
    E-mail: phycw@nus.edu.sg
    Homepage: https://chenweilab.com/

[b] Dr. Y. Liu, Dr. X. Lian, Y. Niu, Dr. J. Yang, Y. Ding, Prof. Dr. W. Chen
    Department of Chemistry,
    National University of Singapore,
    3 Science Drive 3, Singapore 117543, Singapore
    E-mail: yjlchem@nus.edu.sg

[c] Dr. X. Lian
    Centre for Advanced 2D Materials,
    National University of Singapore,
    6 Science Drive 2, Singapore 117546, Singapore

[d] Dr. X. Yu
    Singapore Synchrotron Light Source,
    National University of Singapore,
    5 Research Link, Singapore 117603, Singapore

[e] Prof. Dr. W. Chen
    Department of Physics,
    National University of Singapore,
    2 Science Drive 3, Singapore 117542, Singapore

[**] HATCN = 1,4,5,8,9,11-hexaazatriphenylenehexacarbonitrile

    Supporting information for this article is available on the WWW under https://doi.org/10.1002/batt.202300351

    An invited contribution to a Special Collection on Young Scientists in Battery Research.

Batteries & Supercaps

Research Article
doi.org/10.1002/batt.202300351

Chemistry Europe

European Chemical
Societies Publishing

resulting in continuous electrolyte and anode consumption.[6] On the other hand, the uncontrollable growth of dendrites poses other issues of forming inactive alkali metal regions and exerting significant mechanical pressure, which can ultimately breach the separator and result in short circuits and safety concerns.[7] To address these challenges, various strategies have been developed, such as optimizing electrolyte compositions, establishing anode deposition hosts, and fabricating artificial protective layers.[8]

Based on these strategies, a wide range of protective materials have been employed to stabilize alkali metal anodes (AMAs), including nitrogen-containing materials, which are commonly used in both lithium metal anodes (LMAs) and sodium metal anodes (SMAs). As SEI layers are formed by the direct reaction between AMAs and electrolyte compositions, the addition of appropriate additives can significantly improve the reaction process, leading to the generation of a stable SEI.[9] Through electrolyte composition optimization, additives with nitrogen-containing functional groups, such as CTAB,[10] are reported to anchor metal ions and modify their solvation structures effectively. Additionally, these additives can interact with AMAs to form favorable nitrogen-rich SEIs, as exemplified by LiNO$_3$,[11] C$_{60}$(NO$_2$)$_6$,[12] and TEGDN.[13] Moreover, constructing anode hosts is also a valuable approach to accommodate the substantial volume expansion during cycling and reduce local current density. Anode hosts with high ionic conductivity, low deposition overpotential, large surface area, and superior structural stability have proven beneficial.[14] For instance, nitrogen-doped carbon-based frameworks like NGM,[15] PN-G,[16] N/O-CC,[17] and 3DP-NGA[18] exhibit enhanced lithiophilicity/sodiophilicity due to nitrogen doping, making them highly effective anode deposition hosts. In addition, fabricating artificial protective layers on AMAs is effective to reduce undesirable reactions between the anode and electrolyte by impeding their direct contact, and these layers help regulate a uniform metal ion flux through their homogeneous composition and structure.[3b,19] Nano-porous and highly lithiophilic/sodiophilic g-C$_3$N$_4$ has emerged as an effective artificial protective layer in this context.[20] Moreover, flexible and mechanically stable polymers containing nitrogen functional groups are also favored, such as polythiourea,[21] and polyacrylonitrile.[22]

While recent studies have shown significant improvements in battery performance using nitrogen-containing materials, the relevant studies are still rare and result-oriented which primarily concentrate on battery performance, giving less emphasis to comprehending the fundamental interactions between AMAs and those protective materials. Furthermore, the protective materials recently reported for use in SMBs are often adapted from those used in LMBs. However, it is crucial to recognize that the effectiveness of the similar protective material may differ significantly in SMBs owing to the higher reactivity of sodium metal.[23] For example, the imitated electrolyte additive (Na$_2$S$_6$-NaNO$_3$) exhibits an adverse effect in SMBs, which contrasts with the earlier observations (Li$_2$S$_6$-LiNO$_3$) in LMBs.[24] In this context, to delve deeper into the potential application of nitrogen-containing protective materials in AMAs, conducting a systematic mechanism study to understand the underlying interaction processes between lithium/sodium metal and nitrogen-containing functional groups becomes of utmost importance.

1,4,5,8,9,11-hexaazatriphenylenehexacarbonitrile (HATCN) has garnered attention as a prospective electrode material for use in lithium-ion batteries because of its two unique nitrogen-containing functional groups, which contribute to efficient alkali metal storage.[25] Additionally, it can be readily deposited as flat and uniform films on various substrates under ultra-high vacuum (UHV) conditions, making it an ideal molecular model system for studying interaction processes between alkali metals and various nitrogen-containing groups. In this study, we conducted a comprehensive mechanism investigation based on the HATCN model, utilizing *in-situ* photoelectron spectroscopies as the primary characterization methods. Our findings indicate that HATCN molecules exhibit a robust interaction with both Li and Na metals. Upon contact, alkali metal atoms preferentially anchor to the nitrogen atoms in the inner aromatic heterocycles before the outer nitrile groups. Our work also unravels the differing lithiophilicity/sodiophilicity of two different nitrogen-containing groups, offering valuable insights for the rational design of nitrogen-containing protective materials in AMAs.

Results and Discussion

To investigate the interaction processes between nitrogen-containing functional groups and alkali metals (Li/Na) in isolation from complex battery systems, HATCN molecule was selected as the model material. HATCN molecule possesses unique nitrogen-containing functional groups and high alkali metal affinity due to its strong electron-accepting character, and can be readily deposited on diverse substrates under UHV conditions.[26] As shown in Figure 1(a), HATCN molecule contains two types of nitrogen-containing groups: the imine groups in the inner aromatic heterocycles and the outer nitrile groups. The relative signals were characterized through XPS (Figure 1c), containing two kinds of nitrogen and carbon signals in each spectrum consistent with the molecule structure, which agrees with the previous reports.[27] In N 1s region, the signal of imine nitrogen atoms from the inner aromatic heterocycles (N$_{cycle}$) is located at 400.3 eV, and the signal of nitrogen atoms from the outer nitrile groups (C≡N) is located at 399.8 eV, with an area ratio matching the theoretical value of 1:1. Similarly, in C 1s region, two signals were observed: one from the aromatic heterocycles (C$_{cycle}$) located at 286.7 eV, and the other from nitrile groups (C≡N) located at 287.3 eV, with an area ratio matching the theoretical value of 2:1. To explore the lithiophilicity/sodiophilicity of these two functional groups, Li/Na atoms were stepwise deposited on the prepared HATCN films on Si substrate for *in-situ* characterizations (Figure 1b). Prior to metal deposition, the prepared HATCN films on Si substrate were characterized by AFM (Figure S1). It is measured that the thickness of HATCN films is 15.4 nm, and the films are flat and uniform with the average roughness (R_a) of 3.22 nm.

After the preparation of HATCN films on Si substrate, Li atoms were stepwise deposited for *in-situ* characterizations to study the nitrogen-induced interaction process between HATCN
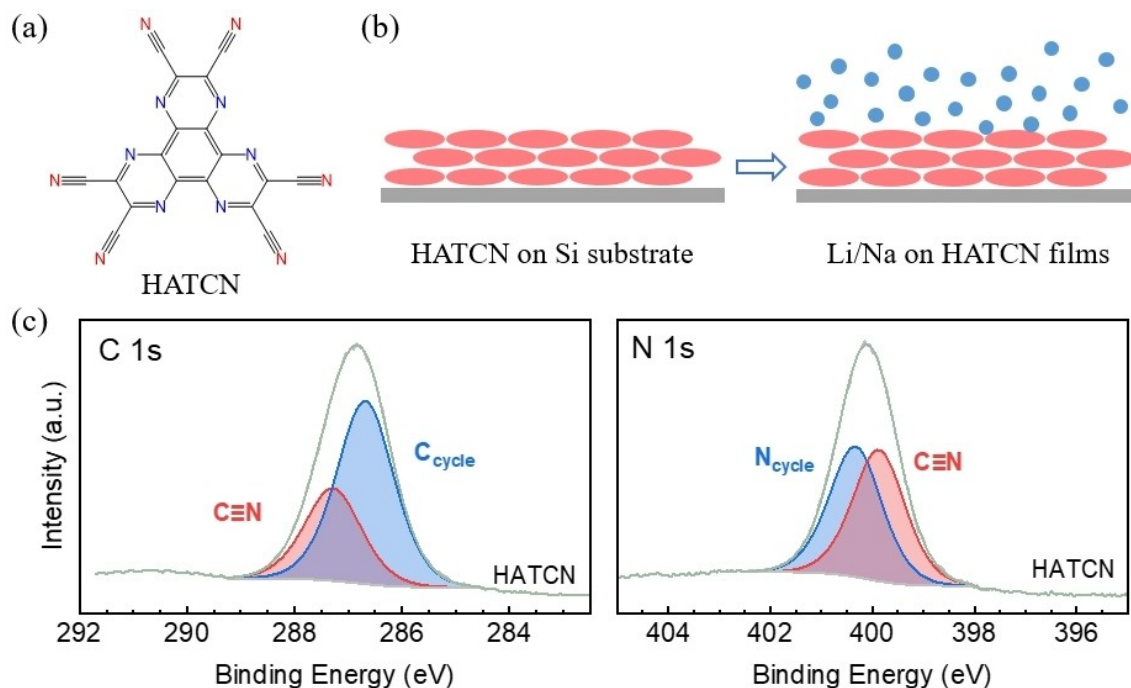
Batteries & Supercaps

Research Article
doi.org/10.1002/batt.202300351

Chemistry
Europe
European Chemical
Societies Publishing

Figure 1. a) HATCN molecular structure. b) Schematic of deposition sequence. c) Characterized XPS spectra of HATCN films deposited on Si substrate.

and Li (Figure 2a). With 0.07 nm Li deposition, the reduced species were observed in N 1s and C 1s spectra. The reduced N species (N_{cycle}–Li) is located at 1.1 eV lower binding energy relative to N_{cycle} species, and the corresponding reduced C species (C_{cycle}–N–Li) is located at 0.6 eV lower binding energy relative to C_{cycle} species. This indicates the first interaction step, in which a small amount of Li atoms reduces the N and C atoms in aromatic heterocycles, generating the reduced species. After that, with 0.3 nm Li deposited, Li atoms continue to interact

with the nitrogen atoms from inner aromatic heterocycles, as indicated by the increase in reduced species (N_{cycle}–Li and C_{cycle}–N–Li) and the decrease in pristine species (N_{cycle} and C_{cycle}). In addition, two new reduced species were observed: the reduced C≡N–Li species located at 1.2 eV lower binding energy for N atoms and CN–Li_x species located at 1.8 eV lower binding energy for C atoms (relative to C≡N species), indicating the interaction of Li atoms and outer nitrile groups. Furthermore, with more Li deposited, it was observed that excess Li atoms
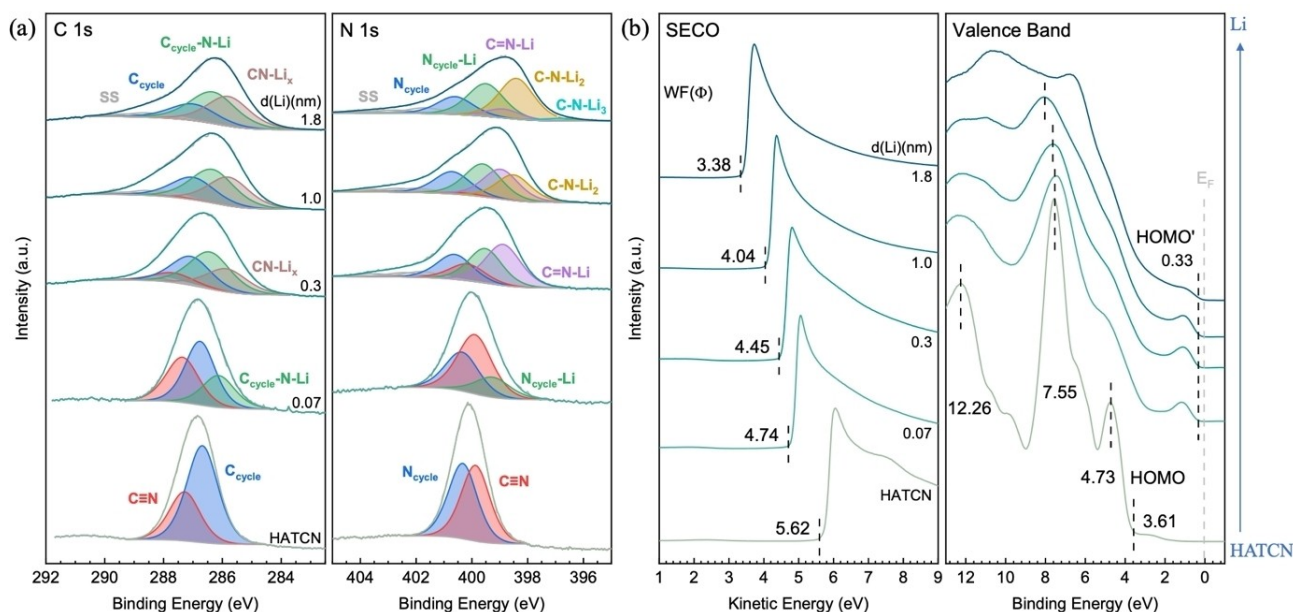

Figure 2. *In-situ* a) XPS core-level and b) UPS spectra of HATCN films with increasing Li deposition.

Batteries & Supercaps

Research Article
doi.org/10.1002/batt.202300351

Chemistry
Europe
European Chemical
Societies Publishing

can further interact with C≡N–Li species, leading to the generation of even more reduced nitrogen species: C–N–Li$_2$ species (1.7 eV lower binding energy relative to C≡N species) and even C–N–Li$_3$ species (3.3 eV lower binding energy relative to C≡N species) in N 1s region. In C 1s region, the corresponding reduced CN–Li$_x$ species becomes gradually stronger with increasing Li deposition. It should be noted that the reduced nitrile carbon species are located at similar binding energy and fitted in a single category (CN–Li$_x$) because carbon atoms are reduced indirectly by receiving electrons from their connected nitrogen atoms, while nitrogen atoms are reduced directly through interaction with Li metal. Besides, with thick Li deposition, the oxidized Li species is detected at 55.9 eV (Figure S2a). Consequently, the nitrogen-induced interaction between HATCN and Li follows a preferential sequence, where Li atoms first interact with the imine groups from inner heterocycles and then with the outer nitrile groups. Moreover, one nitrile group can be reduced by more than one Li atom, suggesting that the interaction between Li and nitrile groups is not limited to a one-to-one ratio.

The electronic structure evolution of HATCN with increasing Li deposition was investigated through *in-situ* UPS (Figure 2b). For pristine HATCN films, the work function value and valence band shape match those in the prior reports, affirming the successful fabrication of pristine HATCN films on the Si substrate.[27a,28] As previously reported, the work function of HATCN films increases with the increasing film thickness due to the different surface dipole, and our prepared HATCN films are thick enough to have the high work function value of 5.62 eV. In addition, the emission from the highest occupied molecular orbital (HOMO) state is clearly distinguished with the onset at 3.61 eV and the maximum at 4.73 eV. Subsequently, as Li deposition increases, the work function experiences a gradual decrease attributed to the charge transfer from Li to HATCN

molecules and the creation of reacted Li-HATCN molecules. In addition, the valence band peaks of pristine HATCN molecules become progressively broader and weaker, indicating the strong interaction between HATCN and Li. Furthermore, a new HOMO state emerged, characterized by an onset at 0.33 eV. This state originates from the occupied lowest unoccupied molecular orbital (LUMO) state of HATCN, resulting from the formation of reacted Li-HATCN molecules, similar to the findings with Al on HATCN.[29]

To explore the interaction mechanism between nitrogen-containing organic materials and SMAs, the *in-situ* XPS study of HATCN films with increasing Na deposition was also conducted (Figure 3a). Analogous to the interaction observed between Li and HATCN, Na atoms similarly interact with the identical sites on HATCN, namely the imine groups in inner aromatic heterocycles and the outer nitrile groups. With thin Na deposition (0.05 nm), two reduced nitrogen atoms and their corresponding reduced carbon atoms can be observed. The reduced nitrogen atoms (N$_{cycle}$–Na and C≡N-Na) are located at 1.1 eV lower binding energy relative to N$_{cycle}$ species and 1.3 eV lower binding energy relative to C≡N species, respectively. As for the corresponding reduced carbon atoms (C$_{cycle}$–N–Na and CN–Na$_x$), they are located at 0.9 eV lower binding energy relative to C$_{cycle}$ species and 2.1 eV lower binding energy relative to C≡N species, which are much lower than that in Li on HATCN, indicating a stronger interaction between Na and these carbon atoms. This can be attributed to the higher reactivity of Na atoms, which allows them to reduce not only the nitrogen atoms but also the connected carbon atoms to a greater extent than Li atoms. Furthermore, it should be noted that, unlike that of Li on HATCN, the interaction sequence of these two nitrogen groups with Na atoms cannot be determined through XPS analysis. Both interaction processes occur simultaneously with thin Na deposition (0.05 nm), indicating that the difference in
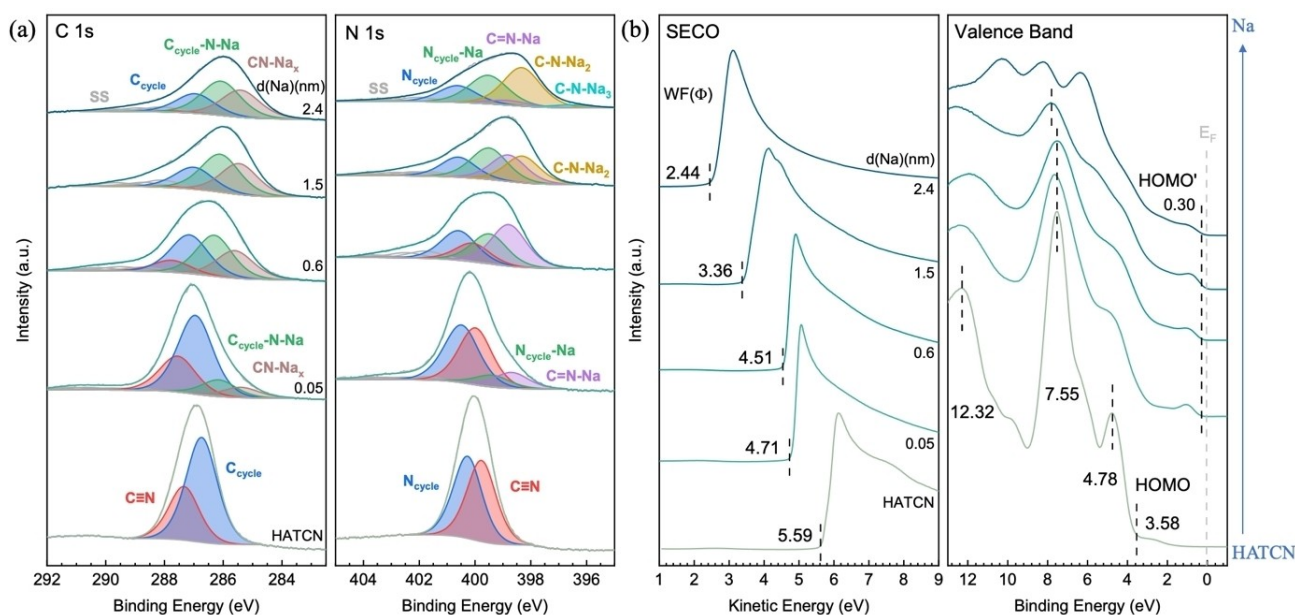

Figure 3. *In-situ* a) XPS core-level and b) UPS spectra of HATCN films with increasing Na deposition.

Batteries & Supercaps

Research Article
doi.org/10.1002/batt.202300351

Chemistry Europe
European Chemical
Societies Publishing

sodiophilicity between these two groups is smaller than the difference in lithiophilicity. After the initial interaction with thin Na deposition, similar to that of Li on HATCN, thicker Na deposition results in the observation of more reduced species (C–N–Na$_2$ and C–N–Na$_3$) because one nitrile group can interact with more than one Na atom. In N 1s region, these reduced nitrogen species are located at 1.8 eV and 3.6 eV lower binding energy relative to C≡N species, respectively. In C 1s region, the corresponding reduced CN–Na$_x$ species is observed to be gradually stronger with increasing Na deposition. Besides, with thick Na deposition, the oxidized Na species is detected at 1072.7 eV (Figure S2b). Consequently, in the nitrogen-induced interaction process between HATCN and Na, Na atoms interact with the same sites as Li on HATCN. However, the interaction strength and metal affinity observed in Na on HATCN differ from those observed in Li on HATCN.

The electronic structure evolution of HATCN films with increasing Na deposition is shown in Figure 3(b). Analogous to the effect of Li on HATCN, the deposition of Na leads to a progressive reduction in the work function of HATCN films. This phenomenon is a result of the charge transfer from Na to HATCN molecules and the formation of reacted Na-HATCN molecules. Furthermore, the strong interaction between HATCN and Na causes the valence band peaks of pristine HATCN molecules to become gradually broader and weaker. Additionally, a new HOMO state was observed with the onset at 0.30 eV, which is produced by the formation of reacted Na-HATCN molecules.

The *in-situ* NEXAFS analysis of HATCN films with increasing Li and Na deposition provides a clearer understanding of the interaction processes between HATCN and alkali metals, including the interaction sequence between two different nitrogen-containing functional groups and Na atoms. As shown

in Figure 4, the C K-edge spectrum of HATCN molecules exhibits two primary peaks. The lower photon energy peak at 285.6 eV originates from the aromatic carbon atoms in inner heterocycles (C$_{cycle}$), while the higher photon energy peak at 286.5 eV originates from the carbon atoms in outer nitrile groups (C≡N).[30] Similarly, the N K-edge spectrum contains two main peaks. According to the calculations in previous studies, the lower photon energy peak located at 398.3 eV has mainly imine (C$_{cycle}$ p$_z$) character, while the higher photon energy peak located at 399.7 eV has mainly nitrile (C≡N p$_{xy}$) character.[27a,30a] Upon alkali metal deposition, *in-situ* NEXAFS analysis shows similar results in Li on HATCN and Na on HATCN. It was observed that the C$_{cycle}$ and N$_{cycle}$ peaks became weaker with thin metal deposition, indicating that alkali metal atoms initially interact with the imine groups in inner aromatic heterocycles, consistent with our XPS results. The formation of the corresponding reduced species was observed from the expanded peak edges in both C and N K-edge spectra. However, the reduced signals are not clearly distinguished as they are obscured by the broad peaks. Subsequently, with increasing metal deposition, the nitrile peaks gradually weaken, and new reduced nitrile signals (B/C/E/F) emerge at the lower photon energy side. Signals B and C primarily originate from the reduced C≡N–Li and C–N–Li$_2$ species, while signals E and F mainly arise from the reduced C≡N–Na and C–N–Na$_2$ species, respectively. The lower photon energies of signals E and F also confirm that Na displays a stronger interaction with HATCN than Li. For signals A and D, they arise from the mixture of reduced N$_{cycle}$ and C≡N species. In C K-Edge region, similar reduced signals are also observed at the slightly smaller photon energy side, but they are not clearly identified due to the indirect reduction of carbon atoms, and the signals are covered by the broad main peak. Consequently, based on the NEXAFS
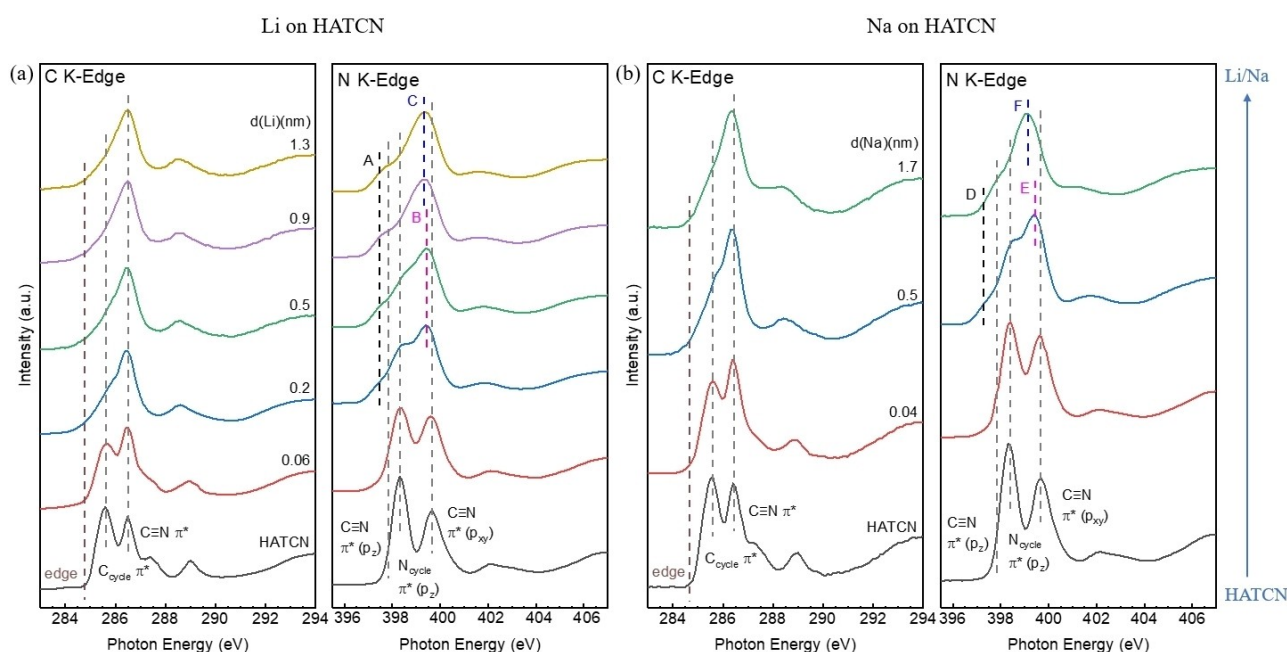

Figure 4. *In-situ* NEXAFS of HATCN films with increasing a) Li and b) Na deposition.

Batteries & Supercaps

Research Article
doi.org/10.1002/batt.202300351

Chemistry Europe
European Chemical
Societies Publishing

results, it can be concluded that the alkali metal atoms initially interact with the imine groups in inner heterocycles and subsequently the outer nitrile groups.

Apart from the *in-situ* mechanism studies discussed above, ex-situ Raman (Figure S3) and AFM (Figure S4) characterizations were carried out to further verify the interaction processes and visually reflect the structural impact of nitrogen-containing groups in HATCN, respectively. These observations suggest the formation of double metal-N sites of M−N≡C and M−N≡C through the interaction between alkali metal atoms and both two kinds of nitrogen groups in HATCN. AFM results also efficiently demonstrate the high uniformity and flatness in the samples after metal deposition, owing to the presence of uniform lithiophilic/sodiophilic groups on the molecular films and the uniform deposition method through alkali metal dispensers.

DFT calculations were also conducted for optimized Li/Na-HATCN structures, which drew a clear and straight picture of the alkali metal interacted HATCN molecules. As shown in Figure 5, when the alkali metal atom interacts with the imine groups in heterocycles, it is anchored by the two neighboring nitrogen atoms at the bay center and has the largest adsorption energy ($\Delta E_{Li1} = -3.44$ eV; $\Delta E_{Na1} = -2.75$ eV), indicating the most favorable interaction site. The second favorable site is the nitrile groups ($\Delta E_{Li2} = -2.81$ eV; $\Delta E_{Na2} = -2.27$ eV). When the alkali metal interacts with the nitrile groups, it is anchored by the two adjacent nitrile nitrogen atoms and located at the corner center. In addition, it is noted that the adsorption energy difference of

these two optimized structures is smaller in the Na-HATCN molecules than that in the Li-HATCN molecules, which can further verify that these two nitrogen-containing functional groups have a smaller sodiophilicity difference than lithiophilicity difference. The last favorable interaction site is the aromatic heterocycles ($\Delta E_{Li3} = -1.47$ eV; $\Delta E_{Na3} = -1.12$ eV). When the alkali metal interacts with the aromatic heterocycle, it is anchored at the center above the cycle. Such interaction process is less likely to occur and could not be detected in our *in-situ* photoelectron spectroscopy experiments.

Moreover, based on the most stable Li/Na-HATCN structure, optimized structures of HATCN with two adsorbed Li/Na atoms were computed (Figure S5). Our results further confirm that imine groups in the inner heterocycles are the most lithiophilic sites, as the second Li atom prefers to interact with them after the first Li atom interacts with the imine groups ($\Delta E_{Li11} = -3.39$ eV). Additionally, it is noticed that after the first Li atom interaction, the opposite and adjacent nitrile groups exhibit similar lithiophilicity with comparable adsorption energy ($\Delta E_{Li12} = -2.54$ eV; $\Delta E_{Li13} = -2.52$ eV). Three additional optimized structures were also calculated, which reveal some rare interaction processes not observed in our *in-situ* study. Similarly, six optimized Na$_2$-HATCN structures were calculated, and similar interaction processes are suggested. However, unlike Li$_2$-HATCN, it should be noted that after the first Na atom interaction, the opposite nitrile groups have higher sodiophilicity than the adjacent nitrile groups, as indicated by the larger adsorption energy ($\Delta E_{Na12} = -1.96$ eV; $\Delta E_{Na13} = -1.76$ eV). This
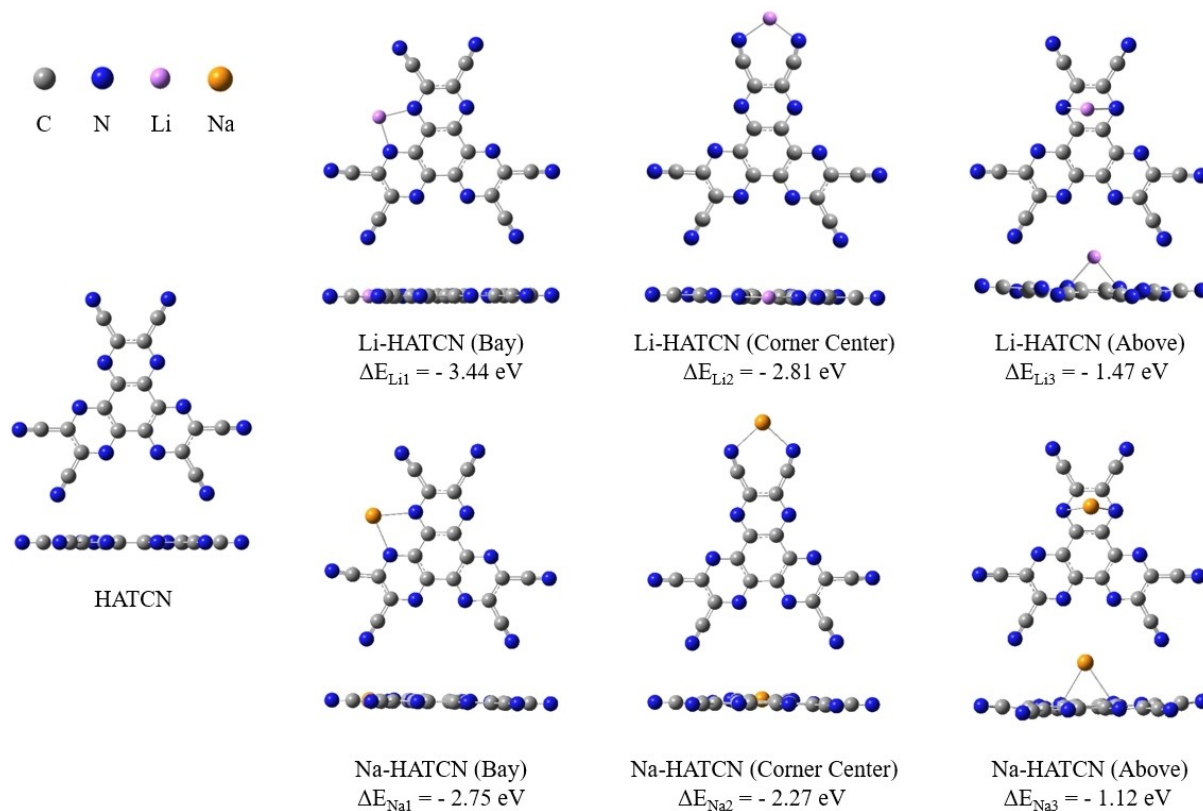

Figure 5. Calculated adsorption energy (ΔE) of optimized Li/Na-HATCN structures.

Batteries & Supercaps

Research Article
doi.org/10.1002/batt.202300351

Chemistry Europe
European Chemical
Societies Publishing

can be attributed to the stronger interaction process between the first Na atom and the imine groups, resulting in the connected carbon atoms becoming more reduced and electron rich. As a result, the opposite nitrile groups become more favorable for interaction with the second Na atom.

Conclusions

In this work, we conducted a mechanism study of the interaction process between HATCN and Li/Na alkali metals mainly based on *in-situ* photoelectron spectroscopies. The interaction process between alkali metals and two different nitrogen-containing functional groups is unraveled. Our findings suggest that both Li and Na atoms follow the same interaction sequence with HATCN molecules: first interacting with the nitrogen atoms at the inner aromatic heterocycles and then at the outer nitrile groups. In addition, with thicker metal deposited, the outer nitrile groups can be reduced by more than one metal atom per group under excess metal deposition. However, a stronger interaction process happens between HATCN and Na metal, and the sodiophilicity difference between the two different nitrogen-containing groups is smaller than the lithiophilicity difference. This study contributes to a more profound comprehension of the interaction process between nitrogen-containing functional groups and alkali metals. Such insights can pave the way for informed design strategies for nitrogen-containing protective materials intended for use with metal anodes.

Methods and Materials

In-situ photoelectron spectroscopies were mainly employed to investigate the interaction mechanism between HATCN and alkali metals (i.e., Li and Na), using a customer-designed UHV-XPS/UPS system.[31] The system comprises both analysis and preparation chambers, enabling direct sample transformation for *in-situ* XPS/UPS analysis. Both chambers operate under UHV conditions, with the analysis chamber pressure below 4×10^{-10} mbar and the preparation chamber pressure below 2.0×10^{-8} mbar.

The preparation of HATCN films and stepwise deposition of alkali metals were performed in the preparation chamber. For the HATCN film preparation, we employed a silicon foil substrate that underwent thorough degassing at 500 °C. HATCN molecules (Luminescence Technology Corp.) were deposited at 240 °C for a duration of 30 minutes, utilizing a resistively heated single Knudsen cell evaporator. The prepared HATCN film was characterized through atomic force microscopy (AFM) to assess its surface morphology and thickness, utilizing a BRUKER Dimension Fast Scan AFM system. After the HATCN film preparation, alkali metals (Li/Na) were stepwise deposited onto the film utilizing an alkali metal dispenser (SAES Getters) with a current of 6.8 A for Li and 4.0 A for Na. The deposition thickness of the alkali metal was estimated through inelastic mean free path (IMFP) calculations, based on XPS core-level intensity difference before and after metal deposition.[32]

The XPS/UPS measurements were conducted through an x-ray source (Omicron DAR400) with Al $K\alpha$ (1486.7 eV) anode, an ultraviolet source (Omicron VUV HIS 13) with He I (21.2 eV), and an electron analyzer (Omicron EA125) with a resolution of 0.05 eV. A

-10 V bias was employed on the sample surface to acquire the secondary electron cut-off (SECO) and measure the work function. For core-level spectra deconvolution, CasaXPS software was employed, utilizing a line shape of GL(50) (50% Gaussian plus 50% Lorentzian function) and a Shirley background. To gain further insights into the interaction processes, *in-situ* NEXAFS was conducted at the K edge of C and N using the SINS beamline of the Singapore Synchrotron Light Source.[33]

Besides the abovementioned *in-situ* experiments, *ex-situ* Raman analysis was performed using a Renishaw InVia Qontor confocal Raman Microscope with a laser excitation wavelength of 785 nm to further corroborate the interaction processes. Initially, pristine HATCN powder was characterized to obtain pure signals. Subsequently, a mixture of HATCN (10 mg) and Li/Na (10 mg) was heated and melted at 300 °C for 15 minutes, following which the resulting products were subjected to Raman testing to assess the impact of the interaction processes. To visually assess the structural impact of nitrogen-containing groups in HATCN, AFM characterization was conducted. Thick HATCN films in their pure form and after metal deposition (for 10 minutes, Li: 6.8 Å; Na: 4.0 Å) were examined using a BRUKER Dimension Fast Scan AFM system.

Alongside experimental investigations, DFT calculations were also performed based on Gaussian 16a software, employing the B3LYP-D3BJ/6-311G(d,p) level of theory.[34] The adsorption energy of the optimized Li/Na-HATCN complex was computed by evaluating the energy difference between the complex and the combined energy of a free metal atom (Li or Na) and a HATCN molecule.

Supporting Information

Surface morphology and thickness of the HATCN film characterized by AFM; XPS spectra of Li/Na 1s of increasing Li/Na metal deposited on HATCN films; Raman spectra of HATCN molecules before and after interacting with alkali metals (Li and Na); AFM characterizations of HATCN films before and after alkali metal depositions; calculated adsorption energy (ΔE) of optimized Li_2/Na_2-HATCN structures; detailed XPS peak fitting parameters for HATCN with increasing Li or Na deposition.

Conflict of Interests

The authors declare no conflict of interest.

Data Availability Statement

Data sharing is not applicable to this article as no new data were created or analyzed in this study.

[1] a) S. Qiao, Q. Zhou, M. Ma, H. K. Liu, S. X. Dou, S. Chong, *ACS Nano* **2023**, *17*, 11220–11252; b) M. Ma, S. Chong, K. Yao, H. K. Liu, S. X. Dou, W. Huang, *Matter* **2023**, *6*, 3220–3273; c) S. Chong, J. Yang, L. Sun, S. Guo, Y. Liu, H. K. Liu, *ACS Nano* **2020**, *14*, 9807–9818.

[2] a) S. Chong, M. Ma, L. Yuan, S. Qiao, S. Dong, H. Liu, S. Dou, *Energy Environ. Mater.* **2022**, *0*, e12458; b) J. Wang, X. Sun, L. Xu, J. Xia, Y. Yang, Z. Yin, F. Luo, Y. Du, *Adv. Mater. Interfaces* **2020**, *7*, 1902168; c) H. Zhao, J. Wang, Y. Zheng, J. Li, X. Han, G. He, Y. Du, *Angew. Chem. Int. Ed. Engl.* **2017**, *56*, 15334–15338; d) Y. Feng, Y. Lv, H. Fu, M. Parekh, A. M. Rao, H. Wang, X. Tai, X. Yi, Y. Lin, J. Zhou, *Natl. Sci. Rev.* **2023**, *10*, nwad118; e) J. Yang, X. Wang, W. Dai, X. Lian, X. Cui, W. Zhang, K. Zhang, M. Lin, R. Zou, K. P. Loh, *Nano-Micro Lett.* **2021**, *13*, 1–14; f) J. Yang, S. Xiao, X. Cui, W. Dai, X. Lian, Z. Hao, Y. Zhao, J.-S. Pan, Y. Zhou, L. Wang, *Energy Storage Mater.* **2020**, *26*, 391–399.

[3] a) S. Yang, X. Min, H. Fan, J. Xiao, Y. Liu, R. Mi, X. Wu, Z. Huang, K. Xi, M. Fang, *J. Mater. Chem. A* **2022**, *10*, 17917–17947; b) T. Wang, Y. Hua, Z. Xu, J. S. Yu, *Small* **2022**, *18*, 2102250.

[4] W. Teng, J. Wu, Q. Liang, J. Deng, Y. Xu, Q. Liu, B. Wang, T. Ma, D. Nan, J. Liu, *Energy Environ. Mater.* **2022**, *6*, e12355.

[5] D. Iermakova, R. Dugas, M. Palacín, A. Ponrouch, *J. Electrochem. Soc.* **2015**, *162*, A7060.

[6] Y. Ji, J. Li, J. Li, *Batteries* **2022**, *8*, 157.

[7] Z. Li, K. Zhu, P. Liu, L. Jiao, *Adv. Energy Mater.* **2022**, *12*, 2100359.

[8] a) J. Yang, M. Li, Z. Sun, X. Lian, Y. Wang, Y. Niu, C. Jiang, Y. Luo, Y. Liu, Z. Tian, *Energy Environ. Sci.* **2023**, *16*, 3837–3846; b) W. Yu, J. Yang, J. Li, K. Zhang, H. Xu, X. Zhou, W. Chen, K. P. Loh, *Adv. Mater.* **2021**, *33*, 2102083.

[9] C. Bao, B. Wang, P. Liu, H. Wu, Y. Zhou, D. Wang, H. Liu, S. Dou, *Adv. Funct. Mater.* **2020**, *30*, 2004891.

[10] J. Luo, Y. Zhang, E. Matios, P. Wang, C. Wang, Y. Xu, X. Hu, H. Wang, B. Li, W. Li, *Nano Lett.* **2022**, *22*, 1382–1390.

[11] F. Wang, Z. Wen, Z. Zheng, W. Fang, L. Chen, F. Chen, N. Zhang, X. Liu, R. Ma, G. Chen, *Adv. Energy Mater.* **2023**, *13*, 2203830.

[12] P. Li, Z. Jiang, X. Huang, X. Lu, J. Xie, S. Cheng, *Nano Energy* **2021**, *89*, 106396.

[13] Z. Wang, Y. Wang, L. Shen, Z. Jin, H. M. Law, A. Wang, W. Wang, F. Ciucci, *Energy Environ. Sci.* **2023**, *16*, 4084–4092.

[14] a) C. Chu, R. Li, F. Cai, Z. Bai, Y. Wang, X. Xu, N. Wang, J. Yang, S. Dou, *Energy Environ. Sci.* **2021**, *14*, 4318–4340; b) Y. Feng, A. M. Rao, J. Zhou, B. Lu, *Adv. Mater.* **2023**, *35*, 2300886.

[15] Y. Liu, C. He, J. Bi, S. Li, H. Du, Z. Du, W. Guan, W. Ai, *Small* **2023**, 2305964.

[16] H. Wang, C. Wang, E. Matios, J. Luo, X. Lu, Y. Zhang, X. Hu, W. Li, *Energy Storage Mater.* **2020**, *32*, 244–252.

[17] H. Liu, M. Osenberg, L. Ni, A. Hilger, L. Chen, D. Zhou, K. Dong, T. Arlt, X. Yao, X. Wang, *J. Energy Chem.* **2021**, *61*, 61–70.

[18] H. Yang, H. Wang, W. Li, B. Tian, T. Xu, D. Kong, S. Huang, K. Liu, X. Li, H. Y. Yang, *J. Mater. Chem. A* **2022**, *10*, 16842–16852.

[19] G. Lu, J. Nai, D. Luan, X. Tao, X. W. Lou, *Sci. Adv.* **2023**, *9*, eadf1550.

[20] J. Wu, L. Tian, H. Duan, Y. Cheng, L. Shi, *ACS Appl. Mater. Interfaces* **2021**, *13*, 46821–46829.

[21] X. He, Z. Liu, Y. Yang, Z. Wang, Y. Chen, Q. Zhang, Z. Shi, Y. Tan, X. Yue, Z. Liang, *J. Mater. Chem. A* **2023**, *11*, 10155–10163.

[22] T. Zhang, X. Li, X. Miao, R. Sun, J. Li, Z. Zhang, R. Wang, C. Wang, Z. Li, L. Yin, *ACS Appl. Mater. Interfaces* **2022**, *14*, 14264–14273.

[23] H. Wang, E. Matios, J. Luo, W. Li, *Chem. Soc. Rev.* **2020**, *49*, 3783–3805.

[24] a) H. Wang, C. Wang, E. Matios, W. Li, *Angew. Chem.* **2018**, *130*, 7860–7863; b) W. Li, H. Yao, K. Yan, G. Zheng, Z. Liang, Y.-M. Chiang, Y. Cui, *Nat. Commun.* **2015**, *6*, 1–8.

[25] a) Y. Wang, P. Poldorn, Y. Wongnongwa, S. Jungsuttiwong, C. Chen, L. Yu, Z. Wang, L. Shi, Y. Zhao, S. Yuan, *Adv. Funct. Mater.* **2022**, *32*, 2111043; b) K. Nakao, Y. Kamakura, M. Fujiwara, T. Shimizu, Y. Yoshida, H. Kitagawa, Y. Yoshikawa, Y. Kitagawa, D. Tanaka, *Cryst. Growth Des.* **2021**, *22*, 26–31.

[26] a) K. Müller, N. Schmidt, S. Link, R. Riedel, J. Bock, W. Malone, K. Lasri, A. Kara, U. Starke, M. Kivala, *Small* **2019**, *15*, 1901741; b) S.-Y. Won, J.-H. Kim, H. Kim, J. K. Yoon, S.-J. Kahng, Y.-K. Kwon, Y. Park, *J. Phys. Chem. C* **2013**, *117*, 21371–21375.

[27] a) C. Christodoulou, A. Giannakopoulos, M. Nardi, G. Ligorio, M. Oehzelt, L. Chen, L. Pasquali, M. Timpel, A. Giglia, S. Nannarone, *J. Phys. Chem. C* **2014**, *118*, 4784–4790; b) E. Oh, S. Park, J. Jeong, S. J. Kang, H. Lee, Y. Yi, *Chem. Phys. Lett.* **2017**, *668*, 64–68; c) T. Zhai, R. Wang, T. Katase, F. Quigley, H. Ohta, P. Amsalem, N. Koch, S. Duhm, *ACS Appl. Electron. Mater.* **2020**, *2*, 3994–4001.

[28] a) Y.-K. Kim, J. Won Kim, Y. Park, *Appl. Phys. Lett.* **2009**, *94*, 43; b) H. Wei, R. Zhang, G. Huang, Y. Yuan, W. Chen, *Opt. Mater.* **2022**, *128*, 112345.

[29] S. M. Park, Y. H. Kim, Y. Yi, H.-Y. Oh, J. Won Kim, *Appl. Phys. Lett.* **2010**, *97*, 176.

[30] a) P. S. Johnson, I. Boukahil, F. Himpsel, K. L. Kearns, J. H. Kang, J.-C. Lin, A. Leugers, G. Meyers, S. Mukhopadhyay, D. H. Jackson, *J. Phys. Chem. C* **2016**, *120*, 1366–1374; b) E. Joo, J. W. Hur, J. Y. Ko, T. G. Kim, J. Y. Hwang, K. E. Smith, H. Lee, S. W. Cho, *Molecules* **2023**, *28*, 3821.

[31] a) Y. Liu, X. Lian, Z. Xie, J. Yang, Y. Ding, W. Chen, *Front. Optoelectron.* **2022**, *15*, 1–12; b) Y. Liu, X. Lian, C. Jiang, Z. Sun, J. Yang, Y. Ding, W. Chen, *Batteries* **2023**, *9*, 21.

[32] C. J. Powell, *J. Electron Spectrosc. Relat. Phenom.* **1988**, *47*, 197–214.

[33] X. Yu, O. Wilhelmi, H. O. Moser, S. V. Vidyaraj, X. Gao, A. T. Wee, T. Nyunt, H. Qian, H. Zheng, *J. Electron Spectrosc. Relat. Phenom.* **2005**, *144*, 1031–1034.

[34] a) M. J. Frisch, G. W. Trucks, H. B. Schlegel, G. E. Scuseria, M. A. Robb, J. R. Cheeseman, G. Scalmani, V. Barone, G. A. Petersson, H. Nakatsuji, X. Li, M. Caricato, A. V. Marenich, J. Bloino, B. G. Janesko, R. Gomperts, B. Mennucci, H. P. Hratchian, J. V. Ortiz, A. F. Izmaylov, J. L. Sonnenberg, Williams, F. Ding, F. Lipparini, F. Egidi, J. Goings, B. Peng, A. Petrone, T. Henderson, D. Ranasinghe, V. G. Zakrzewski, J. Gao, N. Rega, G. Zheng, W. Liang, M. Hada, M. Ehara, K. Toyota, R. Fukuda, J. Hasegawa, M. Ishida, T. Nakajima, Y. Honda, O. Kitao, H. Nakai, T. Vreven, K. Throssell, J. A. Montgomery Jr., J. E. Peralta, F. Ogliaro, M. J. Bearpark, J. J. Heyd, E. N. Brothers, K. N. Kudin, V. N. Staroverov, T. A. Keith, R. Kobayashi, J. Normand, K. Raghavachari, A. P. Rendell, J. C. Burant, S. S. Iyengar, J. Tomasi, M. Cossi, J. M. Millam, M. Klene, C. Adamo, R. Cammi, J. W. Ochterski, R. L. Martin, K. Morokuma, O. Farkas, J. B. Foresman, D. J. Fox, Wallingford, CT, **2016**; b) P. J. Stephens, F. J. Devlin, C. F. Chabalowski, M. J. Frisch, *J. Phys. Chem.* **1994**, *98*, 11623–11627.